Marine Chemistry 219 (2020) 103748

Contents lists available at ScienceDirect

Marine Chemistry

journal homepage: www.elsevier.com/locate/marchem

Dissolved iron in the Bermuda region of the subtropical North Atlantic Ocean: Seasonal dynamics, mesoscale variability, and physicochemical speciation

P.N. Sedwick[a,*], A.R. Bowie[b,c], T.M. Church[d], J.T. Cullen[e], R.J. Johnson[f], M.C. Lohan[g], C.M. Marsay[h], D.J. McGillicuddy Jr[i], B.M. Sohst[a], A. Tagliabue[j], S.J. Ussher[k]

[a] Department of Ocean, Earth and Atmospheric Sciences, Old Dominion University, Norfolk, Virginia 23508, USA
[b] Institute for Marine and Antarctic Studies, University of Tasmania, Hobart, Tasmania 7001, Australia
[c] Antarctic Climate and Ecosystems Cooperative Research Centre, University of Tasmania, Hobart, Tasmania 7001, Australia
[d] School of Earth, Ocean and Environment, University of Delaware, Newark, Delaware 19716, USA
[e] School of Earth and Ocean Sciences, University of Victoria, Victoria, British Columbia V8W 3V6, Canada
[f] Bermuda Institute of Ocean Sciences, St. Georges GE01, Bermuda
[g] Ocean and Earth Science, National Oceanography Centre, University of Southampton, Southampton SO14 3ZH, UK
[h] Skidaway Institute of Oceanography, University of Georgia, Savannah, GA 31411, USA
[i] Woods Hole Oceanographic Institution, Woods Hole, MA 02543, USA
[j] School of Environmental Sciences, University of Liverpool, Liverpool L69 3GP, UK
[k] School of Geography, Earth and Environmental Sciences, University of Plymouth, Plymouth PL4 8AA, UK

ARTICLE INFO

Keywords:
Dissolved iron
Seasonal variability
Physicochemical speciation
Sargasso Sea

ABSTRACT

Water-column data from seven cruises in 2007–2008 reveal pronounced temporal and spatial variations in the distribution of dissolved iron (DFe, < 0.4 μm) over the upper 1000 m of the Sargasso Sea near Bermuda, in the western subtropical North Atlantic Ocean. In near-surface waters, DFe exhibits a clear seasonal cycle, increasing from ~0.1–0.3 nM in spring to ~0.4–1.0 nM in summer-early fall. The observed seasonal ranges appear to reflect the extent of winter convective mixing and of summer dust deposition, both of which are closely tied to atmospheric circulation processes. Surface DFe concentrations also show significant (~two-fold) submesoscale lateral variations during summer, perhaps as a result of lateral inhomogeneities in wet deposition and wind-driven mixing. The summer vertical profiles reveal pronounced DFe minima and sometimes deeper maxima in the lower euphotic zone, which likely reflect biological uptake and shallow remineralization, and eddy-driven lateral gradients in these processes. Significant variability is also seen in the mesopelagic zone, with a DFe concentration range of ~0.4–0.7 nM at 1000 m depth, which may reflect mesoscale isopycnal displacements and/or lateral advection of iron-rich waters in the lower thermocline. Physicochemical iron speciation measurements indicate that the major fraction of DFe that accumulates in surface waters of the Sargasso Sea during summer is colloidal-sized Fe(III), which appears to be complexed by strong, iron-binding organic ligands. Concentrations of soluble iron (sFe, < 0.02 μm) were considerably lower than DFe in the upper euphotic zone during summer, except over the subsurface DFe minima, where sFe accounts for ~50–100% of the DFe pool. Labile Fe(II), on average, accounted for around 20% of DFe, with maximum concentrations of around 0.1 nM in near-surface waters and in the lower thermocline. The seasonal-scale DFe changes that we have documented near Bermuda are of the same magnitude as basin-scale lateral gradients across the North Atlantic, underscoring the importance of time-series observations in understanding the behavior of trace elements in the upper ocean.

1. Introduction

As an essential micronutrient, the transition metal iron modulates marine primary production and the oceanic cycling of carbon and the macronutrient elements (Boyd and Ellwood, 2010; Tagliabue et al., 2017). As such, there is a need to understand the oceanic distribution of dissolved iron (DFe), which is operationally defined by filtration through 0.2 μm or 0.4 μm-pore filters and is assumed to be directly

* Corresponding author.
E-mail address: psedwick@odu.edu (P.N. Sedwick).

https://doi.org/10.1016/j.marchem.2019.103748

Available online 03 January 2020

available to phytoplankton, and the full range of processes that control this distribution. In this regard, new basin-scale data on the oceanic distribution of trace elements that are emerging from the GEOTRACES program (e.g., Mawji et al., 2015; Schlitzer et al., 2018) represent a major advance. For example, recent basin-scale transects in the Atlantic have revealed pronounced lateral gradients in DFe that are thought to reflect deposition of North African soil dust, hydrothermal emissions from the Mid-Atlantic Ridge, sedimentary inputs from the continental margins, and the balance between biological uptake, scavenging and remineralization (e.g., Saito et al., 2013; Ussher et al., 2013; Conway and John, 2014; Rijkenberg et al., 2014; Hatta et al., 2015; Sedwick et al., 2015; Pham and Ito, 2018).

However, such data only provide quasi-synoptic 'snapshots' of water column distributions, which limits their utility in identifying and characterizing time-varying input, removal and internal cycling processes. For DFe, we are lacking the kind of temporally-resolved data sets that have proved critical in understanding the oceanic cycling of macronutrients (e.g., Doney et al., 1996; Karl et al., 1997; Arrigo, 2005; Moore et al., 2013). A limited number of time-series observations have revealed substantial temporal variations in DFe over seasonal and shorter timescales in surface waters of the subtropical (Wu and Boyle, 2002; Boyle et al., 2005; Sedwick et al., 2005; Fitzsimmons et al., 2015a; Hayes et al., 2015), temperate (Bonnet and Guieu, 2006; Birchill et al., 2017) and polar oceans (Sedwick et al., 2000, 2008, 2011; Coale et al., 2005). In order to better define and understand such temporal changes at a mechanistic level, there is a need for sustained time-series observations of iron and other trace elements, together with associated physical and biogeochemical measurements.

Established ocean time-series programs, such as the Bermuda Atlantic Time-series Study (BATS; Steinberg et al., 2001; Lomas et al., 2013) and the Hawaii Ocean Time-series (HOT; Karl and Lukas, 1996; Church et al., 2013) are well suited for collecting such observations. Previous work in the subtropical North Atlantic near Bermuda has documented substantial, seasonal-scale increases in surface DFe concentrations, from relatively low values (~0.1–0.2 nM) in spring to higher values (~0.6–2 nM) in summer, which were suggested to reflect seasonal changes in vertical mixing, biological uptake, particle scavenging and dust deposition (Wu and Boyle, 2002; Sedwick et al., 2005). To better understand this apparent seasonal variability in DFe, we collected samples for iron measurements from the upper water column (≤1000 m) in the BATS region during seven cruises, spanning nearly two full annual cycles, in calendar years 2007 and 2008. Our results delineate a consistent seasonal cycle for DFe in the upper ocean of the BATS region, and reveal significant lateral gradients in DFe concentrations over meso- and submesoscales, as well as providing insights into the physicochemical speciation of DFe during the summer months.

2. Methods

2.1. Study area and sample collection

Located in the western North Atlantic Subtropical Gyre, the Bermuda region of the Sargasso Sea is relatively well studied, as a result of ongoing time-series programs including Hydrostation S, BATS and the Oceanic Flux Program (e.g., Steinberg et al., 2001; Phillips and Joyce, 2007; Lomas et al., 2013; Conte and Weber, 2014). Annual mean surface circulation in the BATS region is characterized by weak geostrophic flow towards the southwest, whereas the westward propagation of mesoscale eddies dominates upper ocean circulation on monthly to seasonal timescales (Siegel et al., 1999; Steinberg et al., 2001; McGillicuddy et al., 2007). A seasonal thermocline and stable, shallow, surface mixed layer are typically present from late spring through early fall, and are eroded by deep convective mixing during the late fall through early spring (Steinberg et al., 2001).

Here we report data from seawater samples and observations that were collected during seven research cruises aboard RV *Atlantic Explorer* between spring 2007 and early fall 2008 (Table 1), as part of the Iron Air-Sea Transfer (FeAST) project. A total of 20 stations were sampled for trace metal measurements in the Sargasso Sea surrounding the BATS region, between latitudes 29°-34°N and longitudes 61°-67°W (Fig. 1). These stations were all located in the deep ocean (> 2000 m water depth), and mostly within mesoscale eddies. The eddies were identified and tracked using sea level altimetry, as described by McGillicuddy et al. (2007). Station locations and associated mesoscale circulation information are provided in Table S1 in the Supplementary Material. Corresponding hydrographic data (temperature, salinity, chlorophyll fluorescence, dissolved oxygen) were collected using the standard BATS conductivity-temperature-depth (CTD) rosette system (Lomas et al., 2013, and references therein). The CTD rosette was deployed directly before or after each trace-metal sampling cast, typically within 1 km of the trace-metal cast location.

Table 1
Details of cruises conducted for the FeAST project aboard RV *Atlantic Explorer*.

Cruise	Cruise period	Water-column DFe stations in area around BATS region
FeAST-1	23–27 April 2007	1–1, 1–2, 1–3
FeAST-2	5–15 July 2007	2–1, 2–2, 2–3, 2–4, 2–5, 2–6
FeAST-3	24–27 September 2007	3–1, 3–2
FeAST-4	5–9 November 2007	4–1, 4–2, 4–3
FeAST-5	28–30 March 2008	5–1
FeAST-6	5–18 June 2008	6–1, 6–6
FeAST-7	21–26 September 2008	7–1, 7–2, 7–3

The water-column samples for trace metal analysis were collected in modified 5 L Teflon-lined external closure Niskin-X samplers (General Oceanics Inc.) that were deployed on a Kevlar line and closed using PVC-coated messengers (Sedwick et al., 2005). Sample depths were estimated from line out as measured by a metering sheave, which introduces an uncertainty of around 10% in collection depths as a result of wire angles of as much as 30° from the vertical. Corresponding surface seawater (0–1 m depth) samples were collected in 1 L wide-mouth low density polyethylene (LDPE) bottles (Nalgene) mounted on the end of a ~5 m bamboo pole. This pole was extended from the ship's stern for sample collection, whilst backing slowly into the wind. Upon recovery, all seawater samples were transferred into a shipboard Class-100 clean container laboratory. In this shipboard clean laboratory, the seawater samples were filtered through either 0.4 μm pore Supor Acropak filter capsules (Pall Corp.), which had been pre-rinsed with ~5 L of ultrapure deionized water (> 18 MΩ cm, Barnstead Nanopure) followed by several hundred mL of each sample (Niskin-X samples), or through 0.4 μm pore Poretics polycarbonate membrane filters (surface samples) mounted in a perfluoroalkoxy alkane (PFA) filtering assembly (Savillex; Sedwick et al., 2005). All filtered seawater samples were acidified to pH 1.7 by adding 4 mL of 6 M ultrapure hydrochloric acid (Seastar Baseline) per liter of sample (i.e., + 0.024 M HCl), and stored in rigorously acid-cleaned 125 mL LDPE bottles (Nalgene) prior to analysis (Sedwick et al., 2005). Additional ~40 mL aliquots were taken from selected filtered water-column samples, and stored at −20 °C in screw-cap polypropylene tubes (Falcon) for post-cruise analyses of dissolved nitrate + nitrite, phosphate and silicic acid, using standard autoanalyzer methods, at the Bermuda Institute of Ocean Sciences or at the Marine Science Institute of the University of California Santa Barbara (nutrient data are presented in Table S2 of the Supplementary Data).

In order to examine lateral gradients in the surface concentrations of dissolved trace metals, near-surface seawater samples were collected along several transects between water-column sampling stations during the two summer cruises (FeAST-2 and FeAST-6; Table 1). Near-surface (~2 m depth) seawater was collected using a trace-metal clean underway 'towfish' system (Bruland et al., 2005; Sedwick et al., 2011) and pumped directly into a shipboard Class-100 'clean bubble'. During these

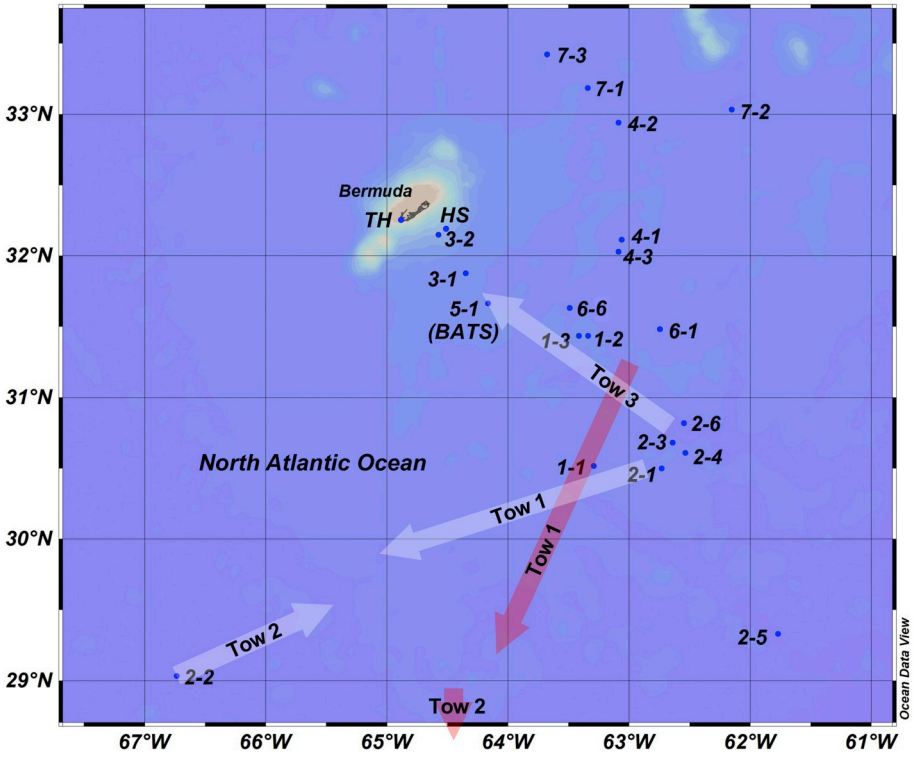

Fig. 1. Map of the BATS region of the Sargasso Sea showing stations where water-column samples were collected for DFe measurements during the FeAST program. Point labelled 1–1 corresponds to cruise FeAST-1, station 1, and so on. Approximate tracks of surface towfish transects are indicated by white arrows for the FeAST-2 cruise, and red arrows for the FeAST-6 cruise. Also shown is the island of Bermuda, and locations of Hydrostation S (HS) the Tudor Hill atmospheric sampling tower (TH). (For interpretation of the references to color in this figure legend, the reader is referred to the web version of this article.)

transects, water samples were collected once every hour, thereby providing near-surface water samples at spacings of ~12 km. These underway seawater samples were filtered using an in-line 0.4 μm-pore Supor Acropak capsule (Pall Corp.), and then acidified with hydrochloric acid and stored in LDPE bottles, as described for the water-column trace metal samples. The FeAST-6 cruise also sampled a number of stations south of 29°N, and collected near-surface underway samples between these stations. The water column data for those FeAST-6 stations are reported by Shelley et al. (2012) and are not discussed here, however the DFe data from the FeAST-6 underway samples south of 29°N will be discussed in relation to the FeAST-2 underway data.

2.2. Sample analysis

Dissolved iron (DFe, < 0.4 μm) was determined in the filtered, acidified seawater samples by flow injection analysis with in-line preconcentration and spectrophotometric detection, modified from the method of Measures et al. (1995) as described by Sedwick et al. (2008). The accuracy of this method was assessed by analysis of reference seawater samples from the SAFe program (all concentrations reported are ± 1 standard deviation): the method used in this study yielded DFe concentrations of 0.11 ± 0.01 nM (n = 15) and 0.97 ± 0.06 nM (n = 14) for SAFe reference seawater S1 and D2, compared with consensus values of 0.093 ± 0.008 nM and 0.933 ± 0.023 nM respectively. Robust estimates of our long-term analytical precision are based on multiple separate determinations of the SAFe seawater reference materials, which yield estimates of intermediate precision (see Worsfold et al., 2019) of ± 15% (n = 33) at the concentration levels of SAFe S and ± 9% (n = 16) at the concentration levels of SAFe D2. The analytical limit of detection is estimated as the DFe concentration equivalent to a peak area that is three times the standard deviation on the system manifold blank, which yields a detection limit below 0.04 nM for a typical manifold blank of < 0.25 nM with a relative standard deviation of 5% (Sedwick et al., 2005). There are also potential blank contributions from the ultrapure hydrochloric acid and ammonium acetate buffer added to each sample, although these were found to be negligible.

In addition, several types of iron speciation measurements were made using samples collected during the summer cruises: soluble iron (sFe, < 0.02 μm) was measured in samples collected during FeAST-2 and FeAST-6; labile iron (II) was determined in samples collected during FeAST-2, and iron-binding ligands were measured in samples collected during FeAST-2. For sFe measurements, seawater samples were filtered as described for DFe, and the filtrate was then filtered through dilute-acid-cleaned, sample-rinsed 0.02 μm Anotop syringe filters using a peristaltic pump (Ussher et al., 2010). The resulting filtrate was acidified to pH 1.7 and stored in acid-cleaned 60 mL LDPE bottles, for post-cruise determinations of sFe by flow injection analysis using the method described for DFe. The analytical accuracy, precision and limit of detection for the sFe measurements are assumed to be the same as for the DFe determinations.

For measurements of iron(II) (Fe(II)), subsamples of unfiltered seawater were drawn directly from the Niskin-X sampler or pole-sample bottle into a 60 mL fluorinated ethylene propylene bottle (Nalgene), typically within 4 h of sampler recovery. Operationally-defined labile Fe(II) (Sarthou et al., 2011) was then measured immediately by flow-injection analysis using in-line preconcentration and chemiluminescence detection (Bowie et al., 2002). The analytical limit of detection was estimated as the Fe(II) concentration corresponding to a signal equal to three times the standard deviation of triplicate analyses of the blank (Bowie et al., 2004; Sarthou et al., 2011), and averaged 5.1 pM. There is currently no standard reference material for Fe(II) in seawater, thus we are unable to provide rigorous estimates of the accuracy and precision of the Fe(II) determinations. However, an indication of the internal instrumental precision for the Fe(II) measurements is provided by repeat measurements of standards prepared in low-Fe(II) seawater, which yielded average relative standard deviations of < 7% for standard additions of 0.2, 0.4, 0.6, 0.8 and 1.0 nM.

Iron-binding ligands were determined shipboard in 0.4 μm-filtered seawater samples using competitive ligand exchange adsorptive cathodic stripping voltammetry (CLE-ACSV), employing 2,3-dihydroxynaphthalene (DHN) as the competing ligand (van den Berg, 2006). Aliquots of seawater samples (10 mL) were dispensed into individual 15 mL perfluoroalkoxy (PFA) vials (Savillex) that were previously

conditioned with seawater/DHN solution. DHN in methanol solution was added to yield a final concentration of 0.5 μM, and iron standard solution was added to the titration vessels to achieve a range of +0 to +8 nM DFe. Samples were then allowed to equilibrate for ~24 h, after which they were transferred to PFA voltammetric cells and 0.5 mL of a potassium bromate/3-(4-(2-hydroxyethyl)-1-piperazinyl)propansulfonic acid/ammonia solution was added to adjust the solution to pH 8 and to provide an oxidant for catalysis of the reaction of Fe-DHN at the hanging mercury drop electrode (HMDE). Labile DFe was determined using a Metrohm model 663VA HMDE connected to a μAutolab II potentiostat (Ecochemie/Metrohm) after purging the sample with nitrogen gas for 5 min followed by 90 s adsorption at −0.1 V, 8 s equilibration and a sampled direct current scan with a frequency of 10 s^{-1} and a step size of 4 mV. Titration data were fitted to a Scatchard or Langmuir type equation to determine relevant thermodynamic parameters and concentrations of DFe complexing ligands (van den Berg, 2006; Cullen et al., 2006).

3. Results and discussion

Vertical concentration profiles for DFe, grouped according to each of the seven FeAST cruises, are presented in Fig. 2a–g, with the corresponding data presented in Table S2 of the Supplementary Data.

3.1. Seasonal changes in dissolved iron

The data from our seven cruises in the BATS region reveal pronounced seasonal-scale changes in DFe concentrations in near surface waters, which increase from ~0.1–0.3 nM during spring to ~0.4–1.0 nM during summer and early fall (Fig. 2). In addition, consistent seasonal changes in the shape of the DFe concentration profiles over the upper 300 m of the water column are apparent. Samples collected during spring (March and April) define a fairly homogeneous DFe distribution over the upper water column (Fig. 2a, e), whereas DFe profiles from the summer (June and July) and early fall (September) are marked by the development of a near-surface concentration maximum, a sub-surface minimum centered at depths of ~75–150 m, and, in some profiles, a deeper sub-surface maximum centered near depths of ~90–150 m (Fig. 2b, c, f, g). The three profiles from the late fall (November 2007; Fig. 2d) show uniformly elevated DFe concentrations over the euphotic zone, as might be expected to result from the seasonal cooling and deepening of the summer mixed layer. At depths > 300 m, DFe concentrations uniformly increase, reaching concentrations of ~0.4–0.7 nM at 1000 m (Fig. 2).

Although there are some significant differences between individual DFe profiles collected during a single cruise (e.g., for FeAST-2 and FeAST-3), a general seasonal pattern remains, as is evident from the cruise-averaged DFe concentration profiles presented in Fig. 2h–n. Evidence to support our interpretation of these general, inter-cruise differences as reflecting temporal rather than spatial variability is provided by water-column DFe profiles from stations 1–3 (sampled on 26 April 2007) and 2–2 (sampled 9 July 2007), shown in Fig. 3a. These profiles represent repeat samplings of a single mode-water eddy that was tracked for several months using sea-level altimetry (Fig. 3b, c). A comparison of the DFe concentration profiles from these two stations (Fig. 3a) clearly indicates the development of a surface maximum, subsurface minimum and subsurface maximum over the 2.5-month period between samplings, assuming Lagrangian behavior for waters within the eddy. Our results thus support and expand on earlier suggestions of a seasonal cycle in DFe that were based on samples collected in the Sargasso Sea during cruises in the spring and summer (Wu and Boyle, 2002; Sedwick et al., 2005).

As noted in these previous studies, such seasonal changes in the vertical distribution of DFe may be interpreted as the result of a number of forcing processes that exhibit well established seasonal changes in the BATS region; namely:

(1) Vertical mixing of the upper water column, which is driven by seasonal changes in surface heat flux and wind stress. In the BATS region, the water column is convectively mixed to ~200–400 m depth during the winter months, then re-stratified by warming during the late spring and into summer, when the surface mixed layer shoals to depths of 20 m or less, before convective overturn again commences in the late fall (Steinberg et al., 2001; Lomas et al., 2013);
(2) Primary production and the associated export of particulate organic matter, which is greatest during the winter-spring period, before nutrients have been exhausted from the upper euphotic zone (Michaels and Knap, 1996; Steinberg et al., 2001; Lomas et al., 2013); and
(3) Deposition of iron-bearing aerosols, which reaches a maximum during the summer months, when high pressure systems over the subtropical North Atlantic region facilitate the atmospheric transport of soil dust from northern Africa to the Sargasso Sea (Moody et al., 1995; Huang et al., 1999; Arimoto et al., 2003; Kadko et al., 2015).

Based on our understanding of the geochemical behavior of iron in the ocean (e.g., Johnson et al., 1997; Boyd and Ellwood, 2010; Tagliabue et al., 2017), the known seasonal modulation of these three processes provides a consistent framework to understand the observed seasonal-scale changes in the vertical distribution of DFe that we have documented in the Sargasso Sea. During the winter and early spring, vertical mixing homogenizes DFe over the upper water column, while primary production removes DFe from the water column through biological assimilation and associated export of organic matter and particle scavenging (Wu and Boyle, 2002; Sedwick et al., 2005). Collectively, these processes result in the relatively low and uniform DFe concentration profiles for our spring cruises (Fig. 2a, e). From late spring into summer, a seasonal thermocline forms together with a shallow surface mixed layer from which macronutrients are depleted by biological uptake, whereas DFe increases as a result of an elevated deposition of mineral aerosols that partially dissolve in surface waters (Sedwick et al., 2005; Fishwick et al., 2014).

In addition, subsurface minima in DFe appear to develop in association with the subsurface chlorophyll maximum (SCM), which typically forms in late spring-early summer and persists into early fall (Fig. 2b, c, f, g). These subsurface DFe minima are typically 10–20 m shallower than the SCM, and may reflect the scavenging removal of DFe by biogenic particles formed in and exported from the lower euphotic zone, as well as the enhanced cellular iron requirements of the phytoplankton that inhabit this low-light environment (Bruland et al., 1994; Sunda and Huntsman, 1997; Sedwick et al., 2005). Alternately, these subsurface DFe minima might be relict features, reflecting the low DFe concentrations in the deeper mixed layer of the winter-spring period that are subsequently isolated from the aeolian input to the shallower surface mixed layer during the summer months (Sedwick et al., 2005).

The latter interpretation is consistent with the DFe profiles from the 2007 FeAST cruises, wherein concentrations in the subsurface DFe minima (Fig. 2b–d) remain similar to those in the spring mixed layer (Fig. 2a). However, the summer profiles from the 2008 cruises (Fig. 2f, g) suggest subsurface depletion in DFe relative to the spring mixed-layer concentrations (Fig. 2e), lending support to the idea that biological uptake and/or scavenging remove DFe from the lower euphotic zone during summer. Moreover, profiles from some of the summer and early fall cruises show DFe maxima at depths below the subsurface DFe minima (Fig. 2b, c, g), consistent with the remineralization or desorption of DFe from particles exported from shallower depths. The three DFe profiles from the single cruise in late fall (Fig. 2d) show uniformly elevated concentrations over the upper 75 m of the water column, consistent with the downward mixing of DFe-rich surface waters that marks the onset of convective overturning.

To calculate the residence time of a dissolved species in a reservoir

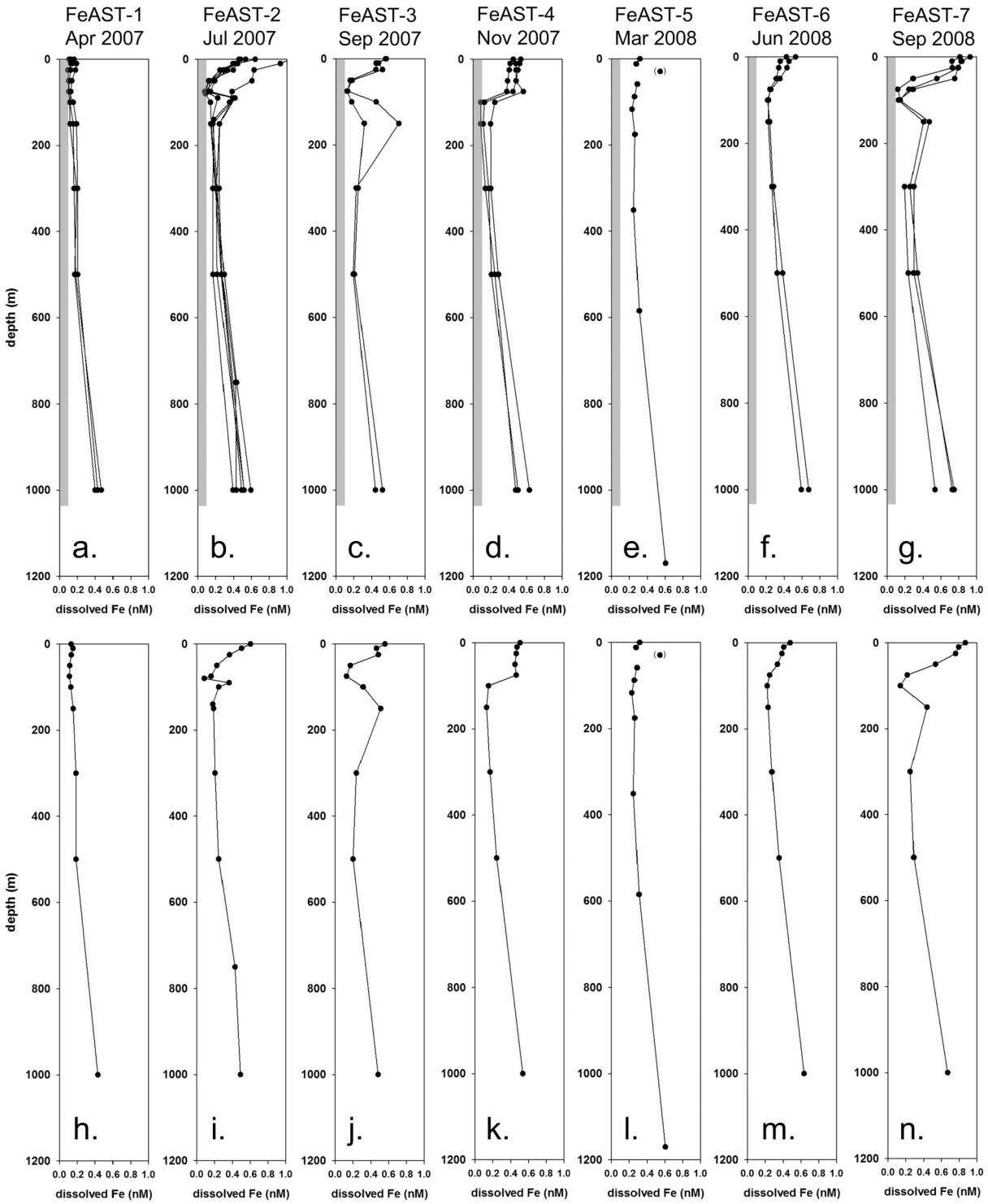

Fig. 2. Top panels: Vertical concentration profiles of DFe from the seven FeAST cruises in 2007–2008 (see Table 1 for cruise dates); the gray bars indicate the 0.1 nM concentration level. Bottom panels: Corresponding profiles showing the average value of DFe concentration versus depth for each of the FeAST cruises. Points in parentheses represent samples for which contamination is suspected.

requires the assumption of steady state, which is clearly not satisfied for DFe in the upper water column in the BATS region over seasonal timescales. However, the upper water column may approach steady state with respect to DFe over sub-seasonal periods in late summer and late winter. If so, then we might use our water column DFe data and estimates of the deposition of water-soluble aerosol iron to compare the residence time of DFe in the upper water column during these periods. For the late summer, using an average DFe concentration of ~0.6 nM in a 20-m thick surface mixed layer, a total aerosol iron deposition of ~100 μmol m^{-2} d^{-1} (Kadko et al., 2015), and a fractional solubility of ~2% for aerosol iron (Sholkovitz et al., 1994) yields a residence time of around one week. The same calculation performed for late winter, assuming a DFe concentration of 0.2 nM over a 100-m thick surface mixed later, a total aerosol iron deposition of ~10 μmol m^{-2} d^{-1} (Kadko et al., 2015), and a fractional solubility of ~20% for aerosol iron (Sholkovitz et al., 1994) yields a residence time near three weeks. These

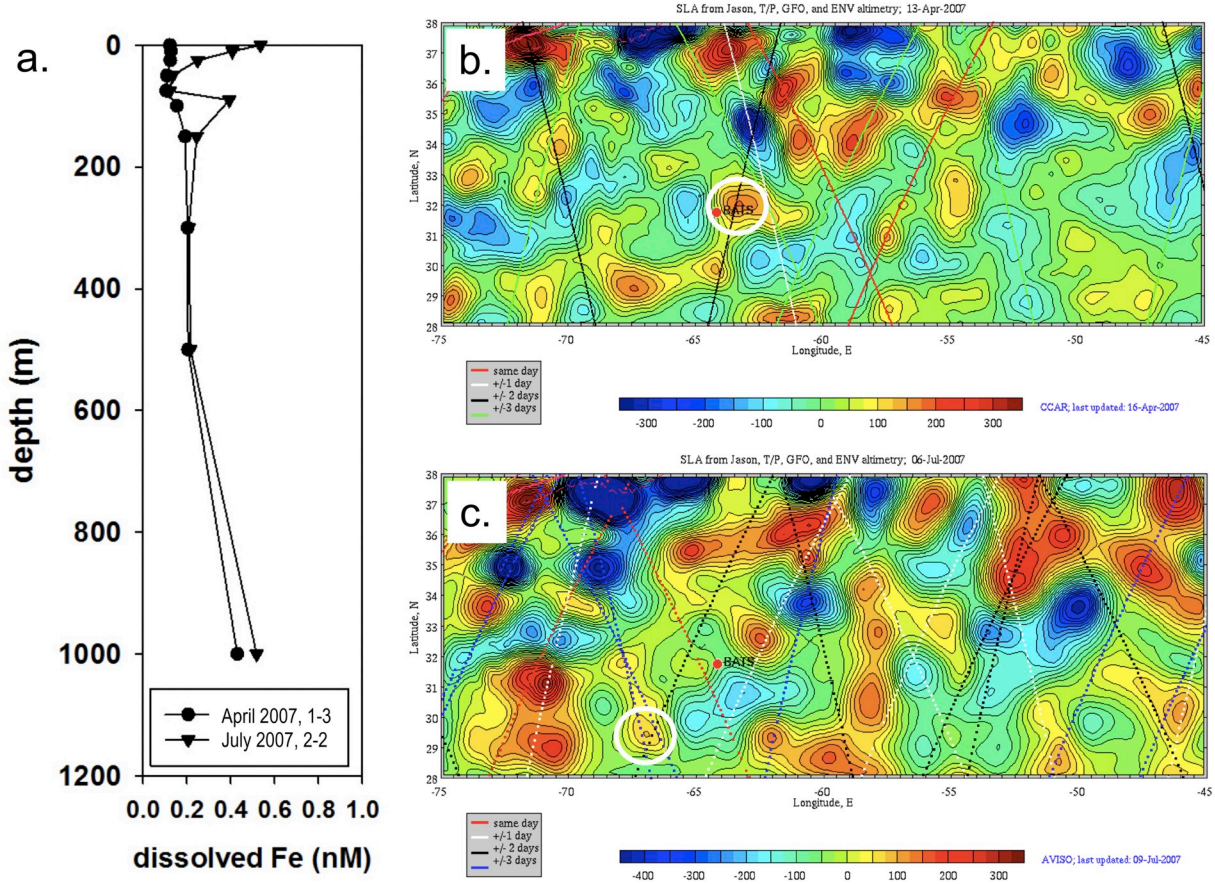

Fig. 3. a. Vertical concentration profiles of DFe in the same mode-water eddy, sampled in April 2007 (station 1–3) and July 2007 (station 2–2). Location of mode-water eddy (white circle) on b. 13 April 2007 (just before FeAST-1) and c. 6 July 2007 (during FeAST-2), overlain on corresponding sea level anomaly maps with color scale in mm (analysis performed using altimeter products produced and distributed by AVISO (www.aviso.oceanobs.com/) as part of the Ssalto ground processing segment).

crude calculations suggest that removal of DFe from the upper water column via particle scavenging and biological uptake is greater in late summer than in late winter, perhaps as a result of enhanced scavenging by aeolian lithogenic particles during summer (e.g., Wuttig et al., 2013), when mineral dust deposition is elevated and biological production is low.

Beyond the apparent seasonal trends in DFe, our water-column profiles from 2007 and 2008 (Fig. 2), together with previously published data from 2003 and 2004 (Sedwick et al., 2005), provide hints of interannual variability, perhaps modulated by year to year differences in the extent of winter mixing, biological production, and mineral dust deposition. For example, the upper water column DFe concentrations in spring 2007 (~0.1 nM, Fig. 2a), are around half the values measured in spring 2008 (~0.2 nM, Fig. 2e), which may reflect the deeper surface mixing and greater net primary production in winter-early spring 2007 compared to winter-early spring 2008 (as revealed by Figs. 1A and 4A in Lomas et al., 2013). In addition, near-surface DFe concentrations as high as 2 nM were measured in the BATS region during summer 2003 (Sedwick et al., 2005), compared with maximum concentrations < 1 nM in summer and early fall of 2007 and 2008 (Fig. 2b, c, f, g). This perhaps reflects a greater total aerosol iron deposition to the Bermuda region during the summer of 2003, which included an intense 'Saharan dust' deposition event in late July-early August (Sedwick et al., 2005).

3.2. Mesoscale variability in the vertical distribution of dissolved iron

As well as the apparent temporal variations in the vertical distribution of DFe in the Sargasso Sea, our field data provide evidence of significant lateral gradients in DFe concentrations at the meso- and submesoscale. During the July 2007 (FeAST-2) and June 2008 (FeAST-6) cruises, water-column and near-surface samples were collected over relatively broad geographic areas. The FeAST-2 cruise collected water-column samples in three different types of eddies – cyclonic (Fig. 1, Stations 2–1, 2–3, 2–4, 2–6), mode-water (Fig. 1, Station 2–2) and anticyclonic (Fig. 1, Station 2–5) – as well as sampling near-surface waters along transits between these eddies. Although water-column DFe data from the FeAST-6 cruise south of 29°N are not discussed here (results are presented by Shelley et al., 2012), we will discuss data from the underway near-surface samples collected from that area during FeAST-6.

The three types of eddies sampled during the FeAST-2 cruise are characterized by distinct hydrographic differences: cyclonic eddies exhibit upward doming of the seasonal and main pycnoclines; anticyclones exhibit depression of both density surfaces; and mode-water eddies have an upward domed seasonal pycnocline, whereas the main pycnocline is depressed (McGillicuddy et al., 2007). Fig. 4 shows schematic depictions of these features, together with a map of satellite-derived sea level altimetry indicating the locations of the three eddies – cyclonic, anticyclonic and mode-water – that were sampled during the FeAST-2 cruise. Fig. 5 shows interpolated vertical quasi-sections of raw temperature and in-situ fluorescence data collected from CTD casts at stations that were occupied along transects across these three eddies during the FeAST-2 cruise. The temperature quasi-section (Fig. 5a) clearly shows the abovementioned pycnocline displacements, whereas the fluorescence quasi-section (Fig. 5b) reveals inter-eddy differences in the depth and intensity of the SCM, which are likely driven by

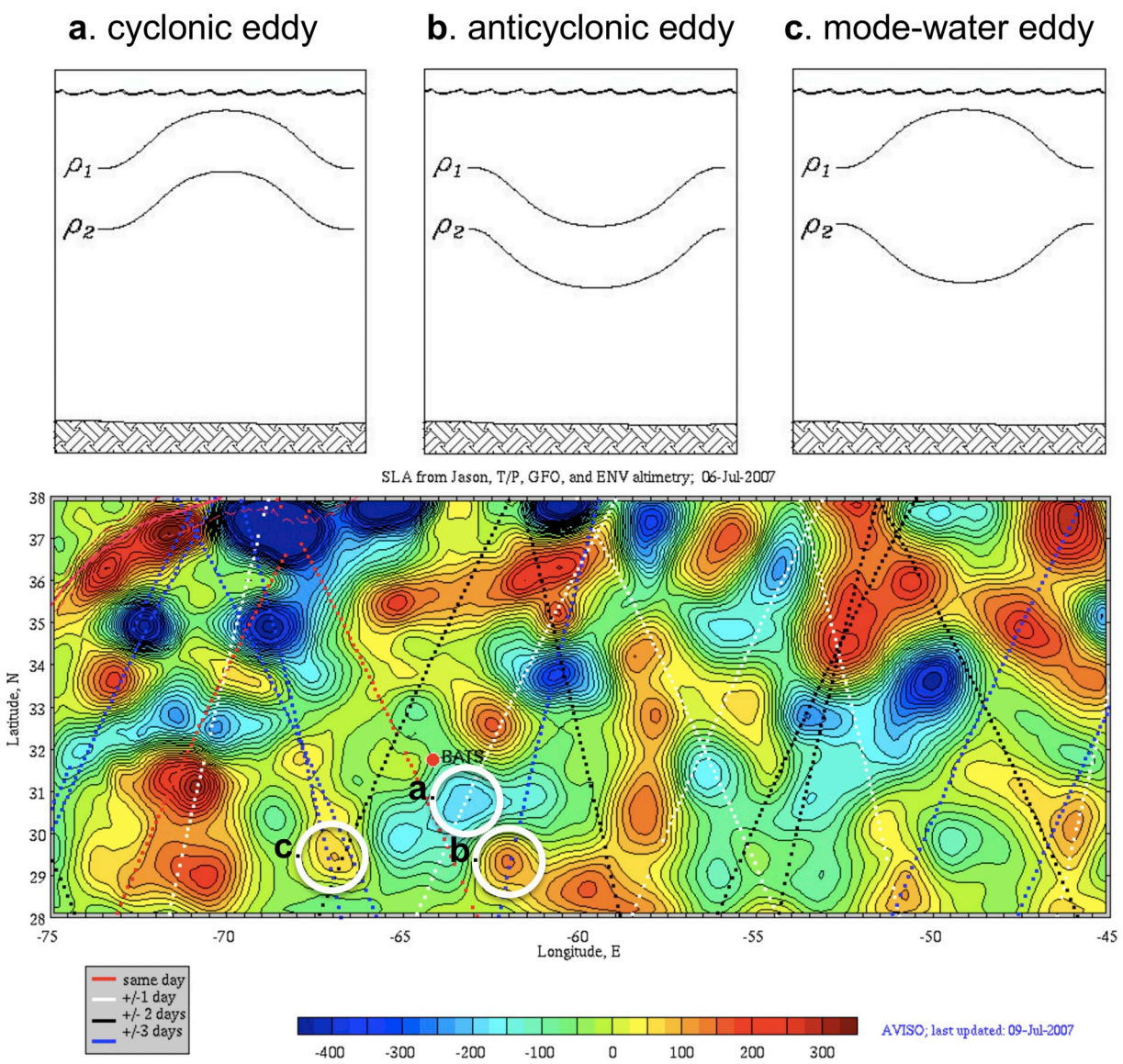

Fig. 4. Schematic cross-section of subsurface isopycnals across a. cyclonic eddy, b. anticyclonic eddy, and c. mode-water eddy (adapted from McGillicuddy et al., 2007). Bottom panel shows locations of each type of eddy (white circles) that was sampled during the FeAST-2 cruise in July 2007, overlain on a map of sea level anomaly from 6 July 2007, with color scale in mm (analysis performed using altimeter products produced and distributed by AVISO (www.aviso.oceanobs.com/) as part of the Ssalto ground processing segment).

differences in vertical nutrient supply.

Both cyclonic and mode-water eddies result in the upwelling of nutrients into the euphotic zone, with eddy/wind interactions amplifying this process for mode-water eddies (McGillicuddy et al., 2007). This likely explains the shallower, more intense SCM observed in these eddy types during the FeAST-2 cruise, particularly in the mode-water eddy, relative to the deeper and weaker SCM in the anticyclonic eddy (Fig. 5b) where the nutricline was depressed (data not shown). Importantly, these inter-eddy differences in fluorescence are reflected in the corresponding DFe profiles (Fig. 6), and are consistent with our interpretation of the subsurface DFe minima as the cumulative result of enhanced biological uptake and scavenging within the SCM. All three eddy types showed surface maxima in DFe, presumably reflecting aerosol iron input. In the cyclonic and mode-water eddies, DFe concentrations decrease to minima at a depth of 75 m, close to the depth of the SCM (Fig. 6, left and middle panels). In the case of the anticyclonic eddy, with its deeper and weaker SCM, a corresponding DFe minimum was not evident and the lowest DFe concentration was measured in the sample from 300 m depth (Fig. 6, right panels).

There are other inter-eddy differences in the FeAST-2 DFe profiles that appear to reflect differences in the hydrographic structures and histories of the eddies. The cyclonic eddy, with its up-doming of the main pycnocline, displays a gradual increase in DFe of ~0.1 nM between 150 m and 500 m depth in three of the four casts. This contrasts with the mode-water eddy, in which there is little change in temperature between these depths, and the corresponding DFe concentrations are indistinguishable (Fig. 6). In addition, the anticyclonic eddy had significantly higher surface DFe concentrations (~1 nM) than the cyclonic and mode-water eddies (~0.5–0.7 nM). This difference likely reflects the back trajectory of the anticyclone, which approached the BATS region from much further south than the cyclonic and mode-water eddies, based on sea level altimetry analyses over the period before the cruise (data not shown). As such, surface waters carried within the anticyclonic eddy are likely to have had relatively high initial DFe concentrations, based on the north-to-south increase in near-surface DFe concentrations revealed by samples collected during the FeAST-6 cruise (as discussed in Section 3.3, below, and by Shelley et al., 2012).

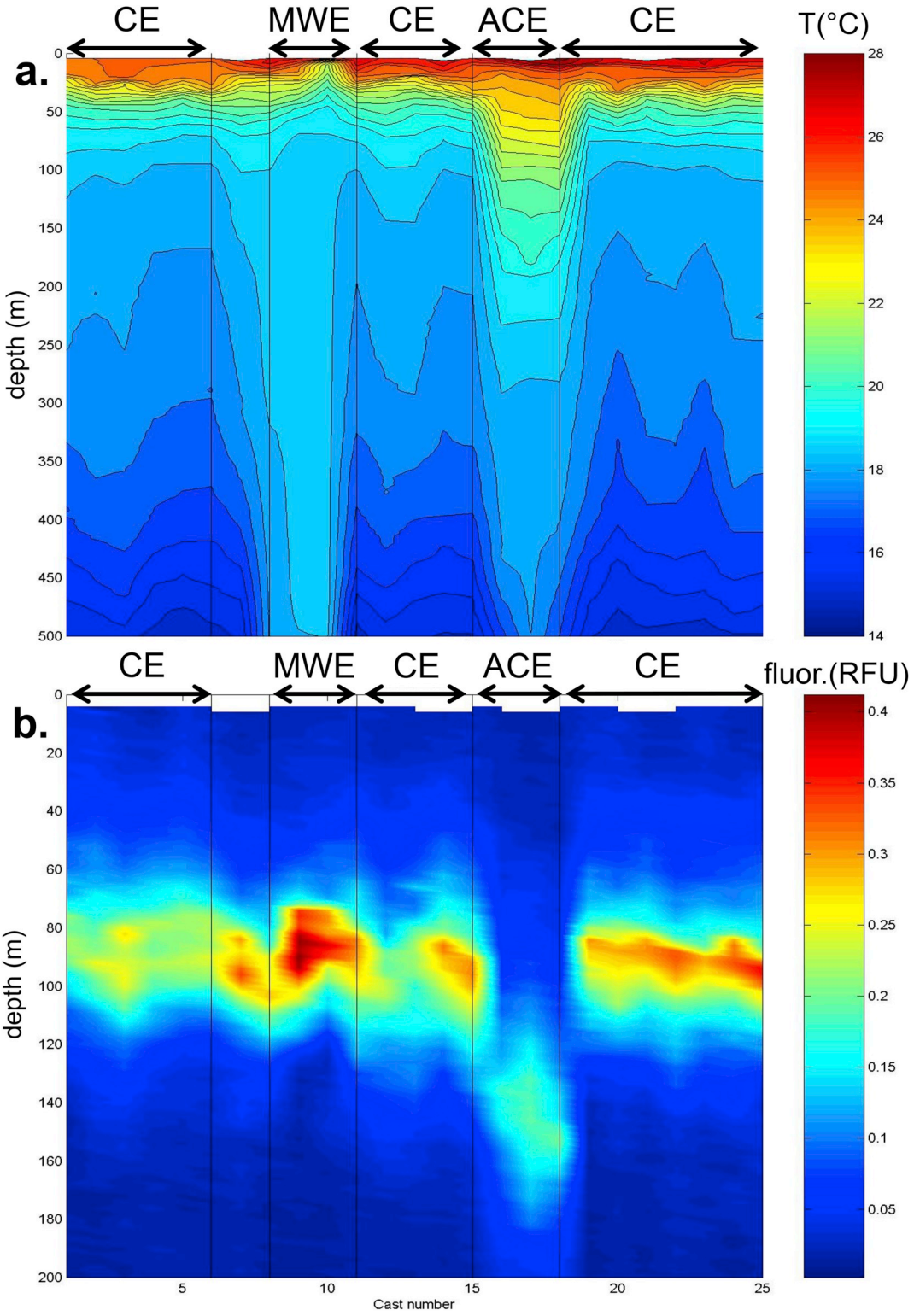

Fig. 5. Vertical quasi-sections of temperature (top; raw data) and in-situ fluorescence (bottom; raw data) from conventional CTD casts conducted across the cyclonic eddy (CE, 3 crossings), mode-water eddy (MWE) and anticyclonic eddy (ACE) that were identified and sampled during FeAST-2 cruise in July 2007. The locations of these eddies are indicated by letters "a", "c", and "b", respectively, in the bottom panel of Fig. 4.

The impact of mesoscale eddies on the depths of isopycnal surfaces extends well below the surface mixed layer and seasonal thermocline. In the CTD profiles obtained nearest to our trace metal sampling casts, temperatures at 1000 m depth varied by as much as several degrees celsius (e.g., compare lower panels in Fig. 6). Our data reveal strong vertical gradients in DFe concentration within the main thermocline between depths of 400 m and 1000 m (Figs. 2, 6). Still higher DFe concentrations are expected at depths below our deepest samples; for example, DFe concentrations above 0.8 nM were measured in the 1200–1500 m depth range at the BATS station in November 2011 (Hatta et al., 2015; Sedwick et al., 2015). Given these vertical concentration gradients, it seems likely that meso- and submesoscale

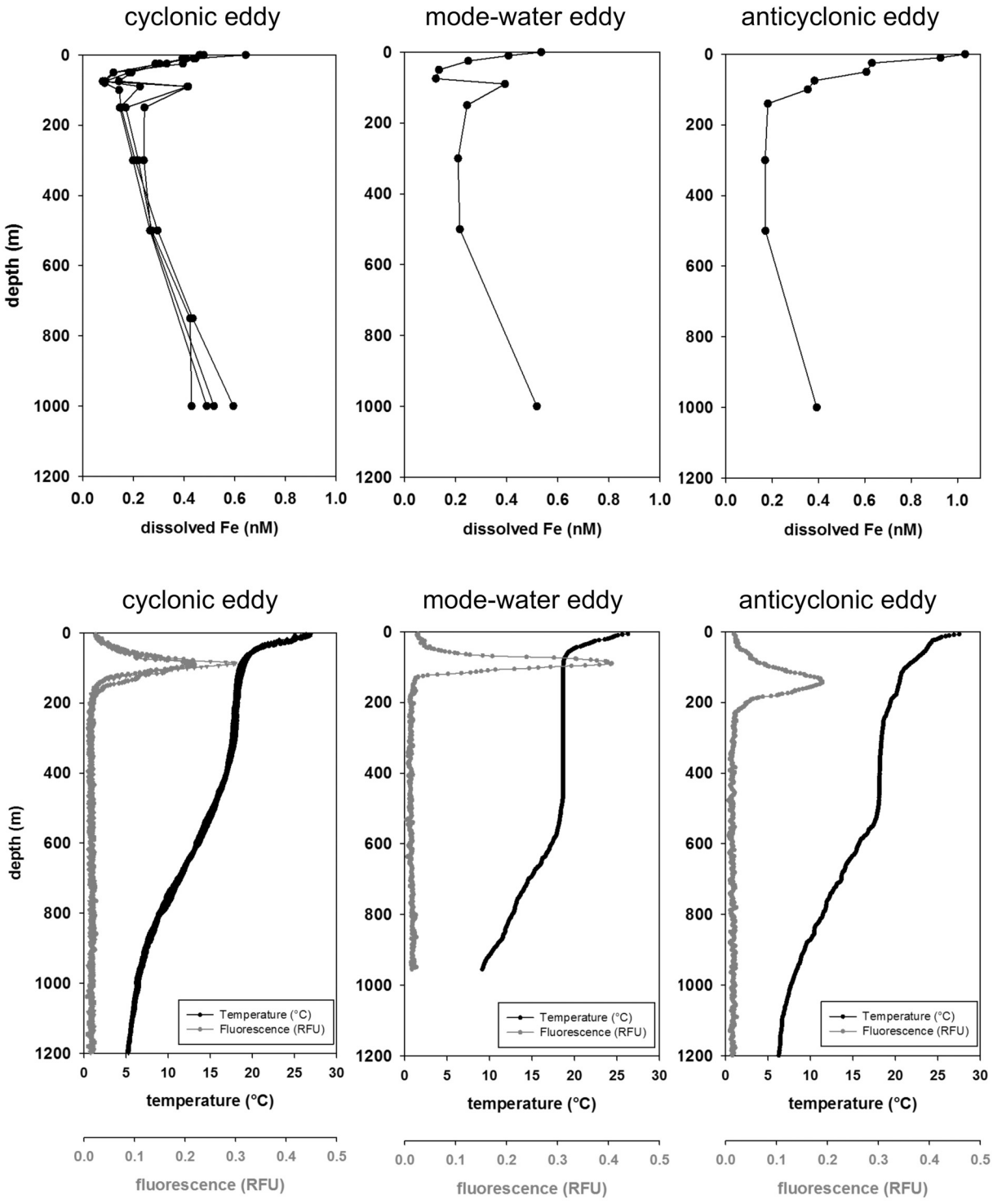

Fig. 6. Water column profiles of DFe concentration (top) and temperature and in-situ fluorescence (bottom) for the three eddies sampled during FeAST-2 cruise in July 2007: cyclonic eddy (left panels, stations 2–1, 2–3, 2–4, 2–6), mode-water eddy (center panels, station 2–2) and anticyclonic eddy (right panels, station 2–5). The locations of these eddies are indicated by letters "a", "c", and "b", respectively, in the bottom panel of Fig. 4.

differences in the depth of isopycnal surfaces contributed to the relatively wide range of DFe concentrations (0.39–0.75 nM) that were measured in samples from 1000 m depth during our two-year study. Unfortunately, we cannot conduct a rigorous examination of DFe as a function of density in our deepest samples, because the Kevlar line samples for DFe were collected as much as ~1 km from the location of the nearest CTD rosette casts (i.e., we lack co-located measurements of DFe concentration and density), and there is also an uncertainty of as much as 10% in our DFe sample depths. An additional factor that may influence the observed variability in the DFe concentrations of our deepest samples is the lateral advection of iron-rich waters from the Bermuda platform or the North American continental margins (Hatta et al., 2015; Conway et al., 2018), a process which has been proposed to explain elevated concentrations of dissolved manganese and particulate lithogenic elements at mesopelagic depths in the Sargasso Sea (Sholkovitz et al., 1994; Conte et al., 2019)

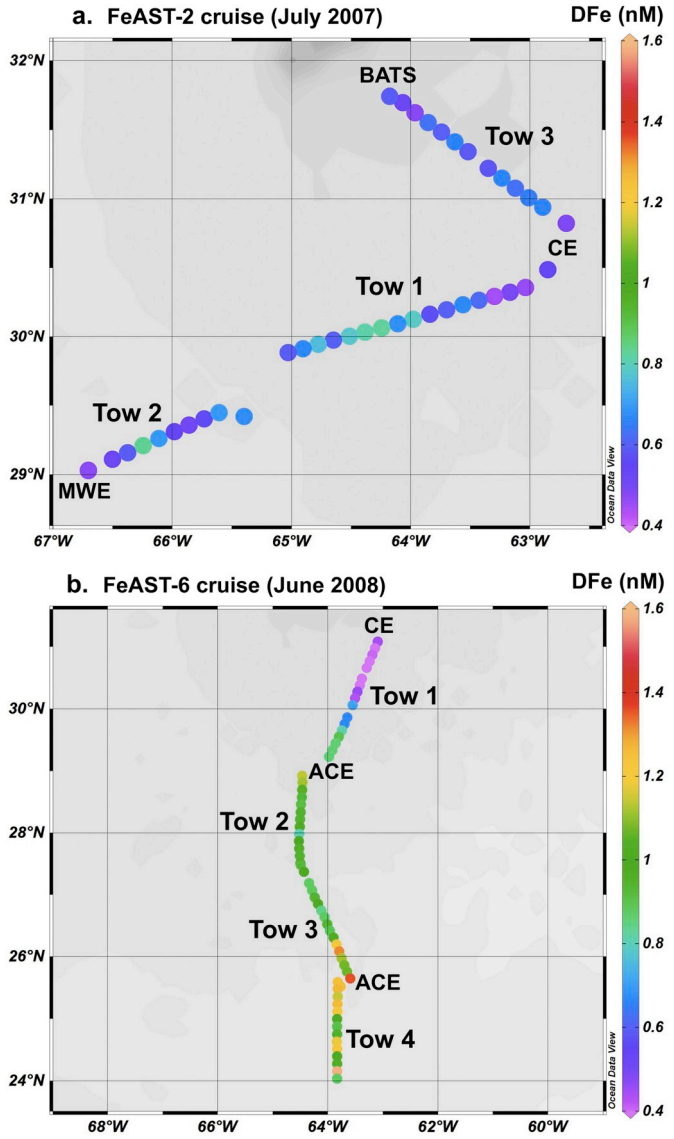

Fig. 7. Map of DFe concentrations in near-surface towfish samples collected during a. FeAST-2 (top) and b. FeAST-6 (bottom) cruises, as well as the approximate locations of mesoscale eddies that were identified and sampled during these cruises (CE = cyclonic eddy; MWE = mode-water eddy; ACE = anticyclonic eddy).

3.3. Lateral variability in near-surface dissolved iron concentrations

Data from underway samples collected during our two summer cruises, FeAST-2 (3 towfish transects, Fig. 7a) and FeAST-6 (4 towfish transects, Fig. 7b), reveal analytically significant variations (> 0.1 nM) in the DFe concentrations of near-surface (~2 m depth) samples over lateral distances of as little as ~10–15 km (samples were collected hourly while underway at ~6–8 knots). For near-surface seawater collected during the FeAST-2 cruise, DFe concentrations display variations of around 0.3–0.4 nM along each towfish transect (Table 2), with DFe differing by > 0.2 nM in some consecutive samples (Fig. 7a). For these samples, there are no discernable trends in near-surface DFe concentrations in relation to sea level anomaly (see Fig. 4), sea-surface temperature, or sea-surface salinity (data not shown), and the mean DFe concentrations along each FeAST-2 towfish transect are similar at around 0.6 ± 0.1 nM (Table 2). It should be noted, however, that the FeAST-2 towfish transects did not cross the anticyclonic eddy, where an elevated surface DFe concentration (Fig. 6) is thought to reflect the south-to-north trajectory of this circulation feature. We suggest that the submesoscale variations in near-surface DFe concentrations along the FeAST 2 towfish transects may reflect lateral inhomogeneities in wet deposition and wind-driven vertical mixing, as a result of the localized rain events and squalls that are often observed during the summer months. Given that DFe concentrations measured in rainwater near Bermuda are as much as two orders of magnitude higher than surface seawater in this region (Sedwick et al., 2007), it is conceivable that spatially patchy rainwater inputs could produce substantial lateral variations in surface DFe concentrations while having little impact on the salinity of surface waters.

Table 2
Range and mean of DFe concentrations in FeAST near-surface seawater towfish samples.

Towfish transect	DFe range	DFe mean ± standard deviation
FeAST-2 tow 1	0.44–0.82 nM	0.63 ± 0.12 nM
FeAST-2 tow 2	0.47–0.83 nM	0.60 ± 0.10 nM
FeAST-2 tow 3	0.47–0.75 nM	0.60 ± 0.07 nM
FeAST-6 tow 1	0.31–0.90 nM	0.59 ± 0.23 nM
FeAST-6 tow 2	0.81–1.13 nM	0.97 ± 0.09 nM
FeAST-6 tow 3	0.84–1.35 nM	1.03 ± 0.16 nM
FeAST-6 tow 4	0.88–1.58 nM	1.13 ± 0.19 nM

Larger lateral differences are apparent from towfish samples collected during the FeAST-6 cruise, with DFe concentrations varying by ~0.3–0.7 nM along each transect (Table 2), and by as much as 0.7 nM between consecutive towfish samples (Fig. 7b). Moreover, the data from the FeAST-6 towfish transects, which span a larger meridional range (~24°-31°N) than the FeAST-2 transects (~29°-32°N), suggest that there is a north-to-south gradient in near-surface DFe concentrations to the south of Bermuda. Although the mean DFe concentration along the northernmost FeAST-6 transect (~0.6 nM, Table 2, tow 1) is not significantly different from the mean values along the FeAST-2 transects, there is an apparent southward increase in DFe concentrations to values above 0.8 nM south of 30°N (Fig. 7b). In addition, the mean near-surface DFe concentrations are significantly higher (0.97–1.13 nM) for the three southernmost towfish transects sampled during the FeAST-6 cruise (Table 2, tows 2, 3 and 4). These observations suggest a regional-scale trend in near surface DFe concentrations, which increase from ~0.6 nM in the BATS region to around 1 nM or more to the south of 29°N. There is no obvious relationship between near-surface DFe concentrations and the mesoscale circulation features that were traversed by the FeAST-6 towfish transects (see Shelley et al., 2012).

The observed lateral variations in near-surface DFe concentrations are most likely driven by differences in mineral aerosol deposition and vertical mixing, and their impact on the DFe inventory of surface waters in our study region, as discussed in Section 3.1. For the individual towfish transects in the BATS region, there were no significant relationships between near-surface DFe concentrations and underway surface salinity or temperature, with the exception of FeAST-6 Tow 1 (Fig. 7), for which there are strong positive correlations between DFe and salinity (r^2 = 0.56) and temperature (r^2 = 0.81). These correlations appear to reflect regional-scale, meridional increases in near-surface DFe, salinity and temperature to the south of the BATS region, rather than patchiness in wet deposition or wind mixing, which would instead be expected to result in negative correlations of DFe with salinity and temperature. As discussed by Shelley et al. (2012), southward increases in the near-surface concentrations of dissolved iron and aluminum likely reflect higher annual dust deposition south of ~30°N (Albani et al., 2014) as well as lessened vertical mixing and biological removal, noting that the region between 25°N and 32°N represents a transition from seasonally-stratified waters in the north to permanently-stratified, oligotrophic waters in the south (Steinberg et al., 2001). Similar increases of ~0.5 nM in surface DFe concentrations between

~30°N and ~20°N in the western subtropical North Atlantic have been reported previously (Wu and Boyle, 2002; Bergquist et al., 2007; Rijkenberg et al., 2014), and Hatta et al. (2015) have noted that there is a positive correlation between surface dissolved iron and aluminum concentrations across the North Atlantic Subtropical Gyre.

3.4. Physicochemical speciation of dissolved iron during summer

Knowledge of the physicochemical speciation of DFe, and its variability in space and time, is key to a mechanistic understanding of numerous processes that impact the ocean iron cycle. These processes include biological uptake, aerosol dissolution, aggregation and disaggregation, sorption and desorption, and interaction with organic matter (Tagliabue et al., 2017). Although the logistical constraints of our cruise program allowed for DFe speciation measurements during only the summer FeAST-2 (July 2007) and FeAST-6 (June 2008) cruises, our results complement other iron speciation data from the Sargasso Sea, including analyses of samples collected from the BATS station during GEOTRACES cruises GA02 (June 2010) and GA03 (November 2011).

3.4.1. Vertical distribution of soluble iron

During the FeAST-2 and FeAST-6 cruises, soluble Fe (< 0.02 μm) concentrations were generally low (< 0.2 nM) throughout the upper water column, and increased to ~0.2–0.3 nM at 1000 m depth (Fig. 8; data provided in Table S2 in the Supplementary Material). The sFe profiles reveal some vertical structure in the euphotic zone, including sFe concentration maxima near the depth of the DFe minima (Fig. 8a–c, e, g, h). However, in discussing these data it should be noted that the analytical uncertainties are relatively large (± 15% or more) for sFe concentrations below 0.1 nM. Several samples for which sFe is greater than DFe are considered contaminated (Fig. 8d, 1000 m sample; Fig. 8e, 300 m sample; Fig. 8f, 75 m sample; Fig. 8g, 10 m sample), while a number of other samples with conspicuously high sFe concentrations may have been contaminated during processing (Fig. 8c, surface sample; Fig. 8f, 10 m and 90 m samples). Consistent with previously reported data from the Sargasso Sea (Wu et al., 2001; Fitzsimmons et al., 2015b), sFe concentrations were considerably lower than DFe in the upper euphotic zone, but account for a substantial proportion (~50–100%) of DFe in the lower euphotic zone, where DFe minima are typically close to maxima in chlorophyll fluorescence (see Fig. 6). Concentrations of both sFe and DFe increase below the euphotic zone, with sFe accounting for 31–56% of DFe concentrations at 1000 m depth.

Our results indicate that the DFe pool is dominated by colloidal iron (cFe, calculated as the difference between DFe and sFe) in near-surface waters, by sFe in the subsurface euphotic zone where DFe concentrations are low, and by significant proportions of both sFe and cFe at

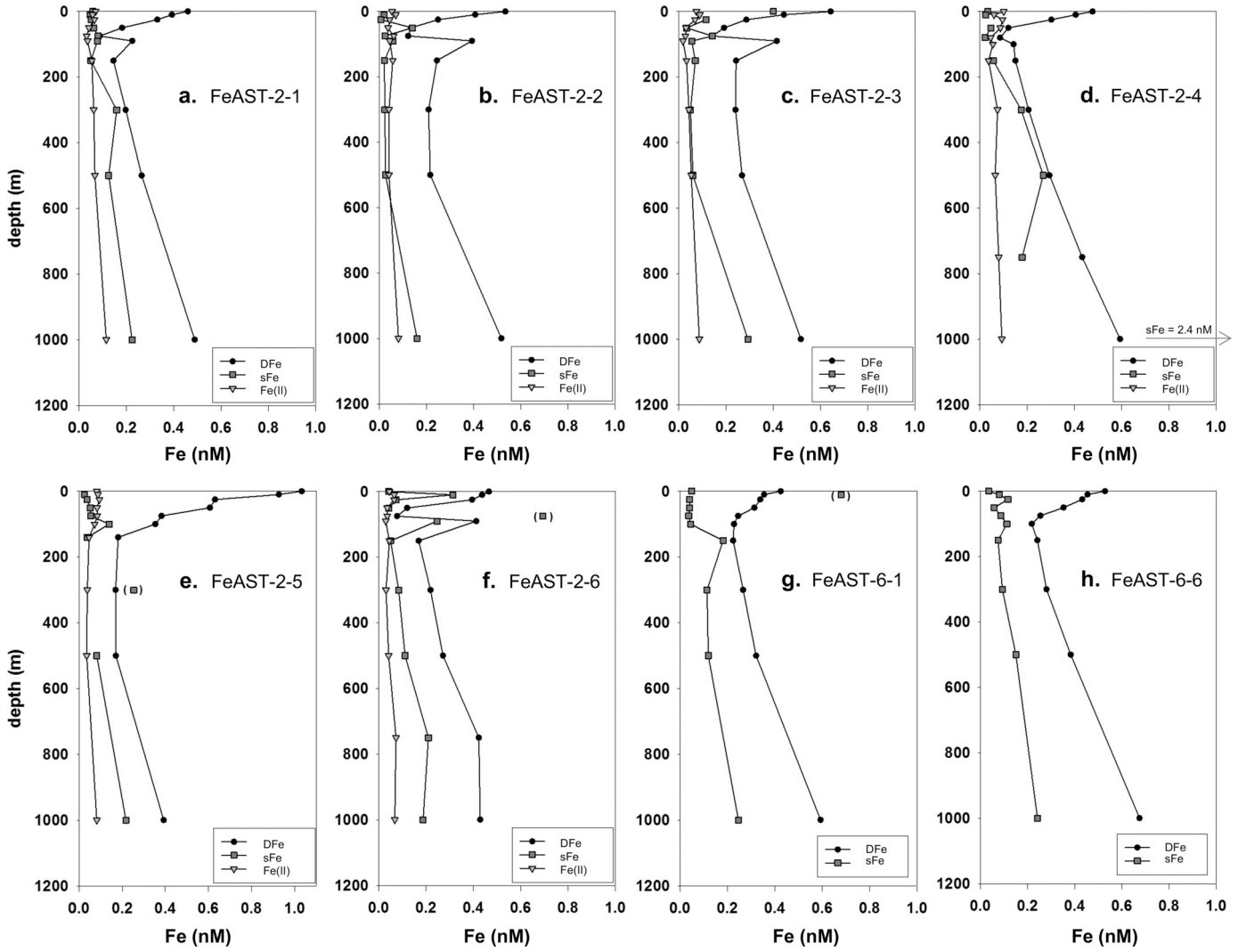

Fig. 8. Vertical concentration profiles of DFe, soluble Fe (sFe) and labile Fe(II) from stations sampled during FeAST-2 and FeAST-6 cruises. Data points shown in parentheses or offscale had measured sFe > DFe, so these sFe samples are considered to have been contaminated.

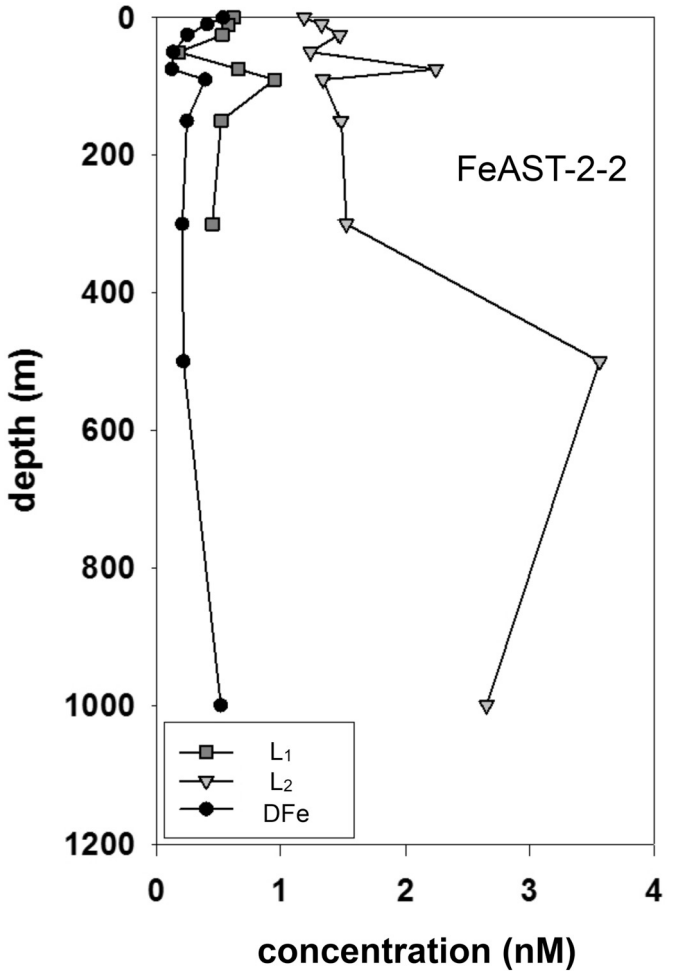

Fig. 9. Vertical concentration profiles of DFe, strong iron-binding ligand (L_1), and weaker iron-binding ligand (L_2) at trace metal station 2 sampled during FeAST-2 cruise.

mesopelagic depths. These observations imply that dust-derived DFe is dominated by colloidal-sized organic and/or inorganic species in near-surface waters, consistent with the results of dissolution experiments using Bermuda aerosols (Fishwick et al., 2014), whereas sFe accounts for a major proportion of DFe in the lower euphotic zone, perhaps due to preferential biological uptake or scavenging removal of cFe, and/or sustained production and biological uptake of sFe from the cFe pool (Bergquist et al., 2007; Fitzsimmons et al., 2015b, 2015c; Birchill et al., 2017). In our deeper samples, sFe and cFe concentrations tend to be more similar, which Fitzsimmons et al. (2015b) ascribe to conditions that approach a steady state, wherein DFe is reversibly exchanged between soluble- and colloidal-size fractions following the remineralization of iron in the mesopelagic zone.

3.4.2. Vertical distribution of Fe(II)

Water column concentrations of labile Fe(II) were generally low during the FeAST-2 cruise (data provided in Table S2 in the Supplementary Material), with maximum values around 0.1 nM measured in samples collected near the surface and in the 750–1000 m depth range (Fig. 8a–f). In general, the low Fe(II) and sFe concentrations are not significantly different over the upper water column, except in the subsurface DFe minima, where Fe(II) does not exhibit the concentration maxima observed for sFe (Fig. 8a–c, e). The elevated Fe(II) concentrations near the sea surface may reflect recent dry or wet deposition of aerosols, which are known to contain readily soluble Fe(II) species (Kieber et al., 2001, 2005; Schroth et al., 2009), or the photochemical reduction of dissolved or particulate Fe(III) species (Barbeau et al., 2001; Hansard et al., 2009). The somewhat elevated Fe (II) concentrations at 750–1000 m depth may reflect remineralization of organic matter, given that apparent oxygen utilization is typically greatest at ~800–900 m depth in our study region, as well as slower rates of Fe(II) oxidation in the cooler waters of the lower thermocline (Millero et al., 1987; Sedwick et al., 2015). The similar concentrations of Fe(II) and sFe above 300 m depth suggest that reduced iron species could comprise a major portion of the sFe pool within the euphotic zone, although our data do not preclude the presence of Fe(II) in the colloidal size range. In addition, we note that Fe(II) complexed by organic ligands would likely be quantified by our analytical method (Ussher et al., 2005), although we cannot determine whether the iron-binding ligands measured by the CLE-ACSV method (see Section 3.4.3, below) would complex Fe(II), in the absence of data concerning the complexation of Fe(II) by the competing ligand DHN.

Dissolved Fe(II) was also measured in 0.2 μm filtered water column samples collected from the BATS station during GEOTRACES cruise GA03, in November 2011 (Sedwick et al., 2015). In this case the concentration profile again showed an elevated Fe(II) concentration (0.25 nM) near the sea surface, with the higher Fe(II) concentration (compared to the FeAST-2 samples) perhaps related to the larger inventory of DFe in the surface mixed layer in November 2011, when DFe concentrations were ~0.7 nM over the upper 100 m of the water column (Sedwick et al., 2015). Below the euphotic zone, the Fe(II) concentrations in the GEOTRACES samples were somewhat higher (0.15–0.24 nM) than the values measured in the FeAST-2 samples. This difference might reflect interannual variability, given that data from the GEOTRACES GA03 section suggests an influence of iron sources on the Bermuda platform and/or North American continental margins on the water column distributions of cFe and DFe at the BATS station (Fitzsimmons et al., 2015b; Hatta et al., 2015; Sedwick et al., 2015; Conway et al., 2018). However, there were also methodological differences in the Fe(II) measurements during FeAST-2 and GEOTRACES GA03, in that the FeAST-2 samples were not filtered, which could conceivably influence the measured Fe(II) concentrations.

3.4.3. Iron-binding ligands

Measurements of dissolved, iron-binding ligands were restricted to a single water column profile from the FeAST-2 cruise in July 2007 (data provided in Table S2 in the Supplementary Material). These results are presented in Fig. 9, which shows vertical concentration profiles of DFe as well as the two iron-binding ligands that were analytically resolved: L_1, a strong iron-binding ligand (logarithm of conditional stability constant = 11.8–12.9), and L_2, a weaker iron-binding ligand (logarithm of conditional stability constant = 10.4–11.0). The vertical profile of L_1 concentrations is quite similar to and exceeds DFe concentrations to a depth of 300 m, below which L_1 was not detected. The weaker ligand, L_2, was substantially higher than DFe, with highest concentrations in the deeper samples. These data indicate that DFe was largely complexed by an excess of strong, iron-binding ligands in the upper water column.

Our results are consistent with other electrochemical measurements of iron-binding ligands in samples collected from the BATS region in June 2010 (Gerringa et al., 2015; Buck et al., 2016) and November 2011 (Buck et al., 2015; Buck et al., 2016; Fitzsimmons et al., 2015c), which used 2-(2-Thiazolylazo)-p-cresol and salicylaldoxime, respectively, as competing ligands. However, there are apparent differences between these data sets in the number and strengths of ligands detected, and in the excess concentrations of these ligands relative to DFe. Possible explanations for these differences, both analytical and environmental, are discussed by Buck et al. (2016), and likely apply to our data as well. In addition, Fitzsimmons et al. (2015c) have examined iron-binding ligands in both soluble and colloidal size fractions in the upper water column at the BATS station, and used thermodynamic calculations to argue that much of the strong ligand-bound iron in the

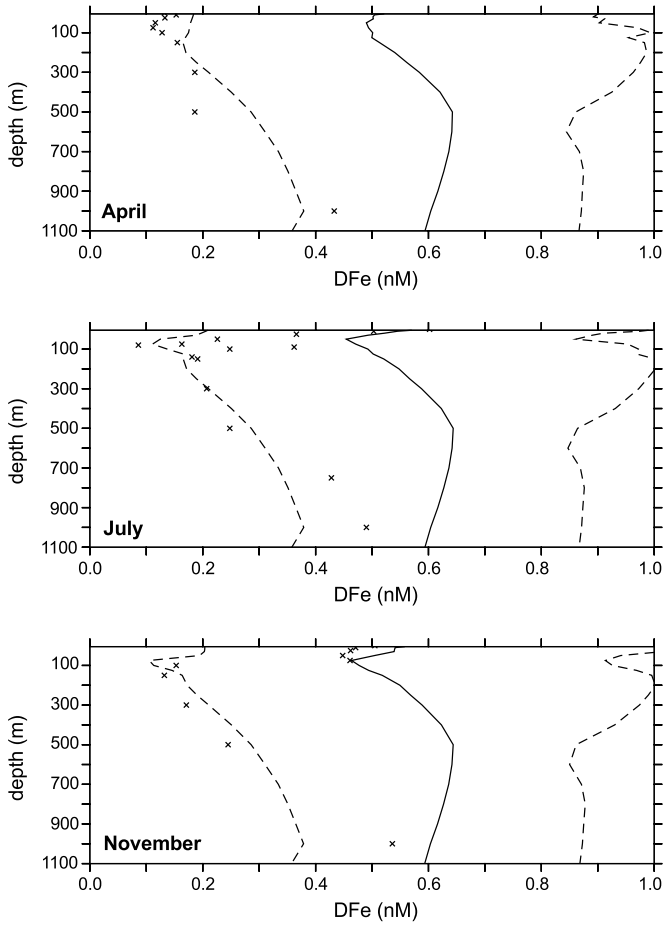

Fig. 10. Multi-model minimum, average and maximum solutions for DFe concentrations at each depth over the upper 1000 m at 31°N, 65°W, for April (top panel), July (middle panel) and November (bottom panel) from the ocean iron model intercomparison project (FeMIP; Tagliabue et al., 2016). Note that these curves show the minimum, average and maximum of all model solutions at each depth, rather than vertical profiles of single-model solutions. Average observed DFe concentrations from the April, July and November 2007 FeAST cruises are also shown as crosses.

euphotic zone might be present as inorganic iron oxyhydroxide species, rather than iron complexed by colloidal-sized organic ligands. Further research will be required to reconcile these observations.

3.5. Implications for biogeochemical modeling of iron in the ocean

Towards the goal of achieving a mechanistic understanding of oceanic iron cycling, time-series observations provide an important metric against which to assess the veracity of ocean biogeochemical models. In the case of dissolved iron, contemporary models are lacking in their ability to reproduce seasonal scale variability in the upper ocean. For example, Fig. 10 shows the seasonal (April, July, November) multi-model minimum, average and maximum solutions for DFe concentrations at each depth over the upper 1000 m at 31°N, 65°W, from the oceanic iron model intercomparison project (FeMIP; Tagliabue et al., 2016). Comparing these FeMIP model solutions to our average DFe profiles for those months in 2007 (Fig. 2h, i, k; data also shown as crosses in Fig. 10) shows the observed DFe concentrations to be substantially less than the multi-model average solutions in subsurface waters, as well as in surface waters during the spring. The multi-model average solutions also show considerably less seasonal variation, compared to our field observations, particularly in the upper water column (< 300 m depth). These discrepancies likely reflect limitations in the model parameterizations of aerosol input and biological removal of DFe in the surface mixed layer, as well as remineralization release and scavenging loss of DFe in subsurface waters.

4. Concluding remarks

Our multi-cruise, seasonal-scale measurements of dissolved iron in the Bermuda region demonstrate substantial temporal and spatial variations in the distribution of this biologically important trace element in the upper ocean. Most striking are the pronounced seasonal-scale changes in the distribution of DFe over the euphotic zone and upper thermocline. Here vertical profiles evolve from the relatively low and homogeneous DFe concentrations (~0.1–0.3 nM) in early spring, to the elevated near-surface concentrations (~0.4–1 nM) and underlying concentration minima near the SCM, which reflect the impact of thermal stratification and elevated mineral aerosol deposition during the summer and early fall. The potential importance of time-series measurements of iron and other trace elements is underscored by recognizing that the seasonal-scale of DFe changes that we observed in the surface ocean near Bermuda are of the same magnitude as the basin-scale lateral gradients in DFe concentrations across the North Atlantic (e.g., Hatta et al., 2015; Rijkenberg et al., 2014), and that such temporal variability may exist in many different oceanic settings (e.g., Bonnet and Guieu, 2006; Birchill et al., 2017).

Our data also reveal significant lateral variations in the distribution of DFe in the Sargasso Sea, which appear to reflect mesoscale physical circulation features and their impact on biological production, as well as submesoscale to regional-scale gradients in the dry and wet deposition of aerosol iron to the ocean surface. Finally, our time-series data highlight the limitations of contemporary ocean biogeochemical models in simulating the vertical distribution and temporal variability of DFe. In this regard, research that links time-series measurements of iron speciation and major physical and biogeochemical variables with the development of mechanistic numerical models offers the possibility to significantly advance our understanding of the ocean iron cycle and its sensitivity to future environmental changes.

Supplementary data to this article can be found online at https://doi.org/10.1016/j.marchem.2019.103748.

Acknowledgements

We thank the officers and crew of RV *Atlantic Explorer*, the numerous scientific participants in the FeAST cruises, and chief scientists Maureen Conte, John Dacey and Carl Lamborg, who allowed us to piggyback our field sampling on their shipboard programs. This research was primarily funded by the US National Science Foundation through awards OCE-0222053, OCE-0138352 and OCE-1829833 (to PNS), and OCE-0222046 (to TMC); PNS and ARB also acknowledge support from the Institute of Marine and Antarctic Studies, the Antarctic Climate and Ecosystems CRC, and the University of Tasmania through a Visiting Scholar award, and SJU acknowledges support provided by a European Commission Marie Curie Fellowship (PIOF-GA-2009-235418 SOLAIROS). Valery Kosnyrev is thanked for preparation of the altimetric analyses, and DJM gratefully acknowledges support from NSF and NASA. Altimeter products were produced and distributed by AVISO (www.aviso.oceanobs.com/) as part of the Ssalto ground processing segment. The authors also thank three anonymous reviewers for their thoughtful comments and suggestions, which have improved the manuscript.

References

Albani, S., Mahowald, N.M., Perry, A.T., Scanza, R.A., Zender, C.S., Heavens, N.G., et al., 2014. Improved dust representation in the community atmosphere model. J. Adv. Model. Earth Syst. 6 (3), 541–570.

Arimoto, R., Duce, R.A., Ray, B.J., Tomza, U., 2003. Dry deposition of trace elements to

the western North Atlantic. Glob. Biogeochem. Cycles 17 (1).
Arrigo, K.R., 2005. Marine microorganisms and global nutrient cycles. Nature 437 (7057), 349–355.
Barbeau, K., Rue, E.L., Bruland, K.W., Butler, A., 2001. Photochemical cycling of iron in the surface ocean mediated by microbial iron (III)-binding ligands. Nature 413 (6854), 409–413.
van den Berg, C.M.G., 2006. Chemical speciation of iron in seawater by cathodic stripping voltammetry with dihydroxynapthalene. Anal. Chem. 78, 156–163.
Bergquist, B.A., Wu, J., Boyle, E.A., 2007. Variability in oceanic dissolved iron is dominated by the colloidal fraction. Geochim. Cosmochim. Acta 71 (12), 2960–2974.
Birchill, A.J., Milne, A., Woodward, E.M.S., Harris, C., Annett, A., Rusiecka, D., et al., 2017. Seasonal iron depletion in temperate shelf seas. Geophys. Res. Lett. 44 (17), 8987–8996.
Bonnet, S., Guieu, C., 2006. Atmospheric forcing on the annual iron cycle in the western Mediterranean Sea: a 1-year survey. J. Geophys. Res. Oceans 111 (C9).
Bowie, A.R., Achterberg, E.P., Sedwick, P.N., Ussher, S., Worsfold, P.J., 2002. Real-time monitoring of picomolar concentrations of iron (II) in marine waters using automated flow injection-chemiluminescence instrumentation. Environ. Sci. Technol. 36 (21), 4600–4607.
Bowie, A.R., Sedwick, P.N., Worsfold, P.J., 2004. Analytical intercomparison between flow injection-chemiluminescence and flow injection-spectrophotometry for the determination of picomolar concentrations of iron in seawater. Limnol. Oceanogr. Methods 2, 42–54.
Boyd, P.W., Ellwood, M.J., 2010. The biogeochemical cycle of iron in the ocean. Nat. Geosci. 3 (10), 675–682.
Boyle, E.A., Bergquist, B.A., Kayser, R.A., Mahowald, N., 2005. Iron, manganese, and lead at Hawaii Ocean Time-series station ALOHA: temporal variability and an intermediate water hydrothermal plume. Geochim. Cosmochim. Acta 69 (4), 933–952.
Bruland, K.W., Orians, K.J., Cowen, J.P., 1994. Reactive trace metals in the stratified central North Pacific. Geochim. Cosmochim. Acta 58 (15), 3171–3182.
Bruland, K.W., Rue, E.L., Smith, G.J., DiTullio, G.R., 2005. Iron, macronutrients and diatom blooms in the Peru upwelling regime: brown and blue waters of Peru. Mar. Chem. 93 (2), 81–103.
Buck, K.N., Sohst, B., Sedwick, P.N., 2015. The organic complexation of dissolved iron along the US GEOTRACES (GA03) North Atlantic Section. Deep-Sea Res. II Top. Stud. Oceanogr. 116, 152–165.
Buck, K.N., Gerringa, L.J., Rijkenberg, M.J., 2016. An intercomparison of dissolved iron speciation at the Bermuda Atlantic Time-series Study (BATS) site: results from GEOTRACES Crossover Station A. Front. Mar. Sci. 3, 262.
Church, M.J., Lomas, M.W., Muller-Karger, F., 2013. Sea change: charting the course for biogeochemical ocean time-series research in a new millennium. Deep-Sea Res. II Top. Stud. Oceanogr. 93, 2–15.
Coale, K.H., Gordon, R.M., Wang, X., 2005. The distribution and behavior of dissolved and particulate iron and zinc in the Ross Sea and Antarctic circumpolar current along 170 W. Deep-Sea Res. I Oceanogr. Res. Pap. 52 (2), 295–318.
Conte, M.H., Weber, J.C., 2014. Particle flux in the deep Sargasso Sea: the 35-year oceanic flux program time series. Oceanography 27 (1), 142–147.
Conte, M.H., Carter, A.M., Koweek, D.A., Huang, S., Weber, J.C., 2019. The elemental composition of the deep particle flux in the Sargasso Sea. Chem. Geol. 511, 279–313.
Conway, T.M., John, S.G., 2014. Quantification of dissolved iron sources to the North Atlantic Ocean. Nature 511 (7508), 212.
Conway, T.M., Palter, J.B., de Souza, G.F., 2018. Gulf stream rings as a source of iron to the North Atlantic subtropical gyre. Nat. Geosci. 11 (8), 594.
Cullen, J.T., Bergquist, B.A., Moffett, J.W., 2006. Thermodynamic characterization of the partitioning of iron between soluble and colloidal species in the Atlantic Ocean. Mar. Chem. 98 (2), 295–303.
Doney, S.C., Glover, D.M., Najjar, R.G., 1996. A new coupled, one-dimensional biological-physical model for the upper ocean: applications to the JGOFS Bermuda Atlantic time-series Study (BATS) site. Deep-Sea Res. II Top. Stud. Oceanogr. 43 (2), 591–624.
Fishwick, M.P., Sedwick, P.N., Lohan, M.C., Worsfold, P.J., Buck, K.N., Church, T.M., Ussher, S.J., 2014. The impact of changing surface ocean conditions on the dissolution of aerosol iron. Glob. Biogeochem. Cycles 28 (11), 1235–1250.
Fitzsimmons, J.N., Hayes, C.T., Al-Subiai, S.N., Zhang, R., Morton, P.L., Weisend, R.E., et al., 2015a. Daily to decadal variability of size-fractionated iron and iron-binding ligands at the Hawaii Ocean Time-series Station ALOHA. Geochim. Cosmochim. Acta 171, 303–324.
Fitzsimmons, J.N., Carrasco, G.G., Wu, J., Roshan, S., Hatta, M., Measures, C.I., et al., 2015b. Partitioning of dissolved iron and iron isotopes into soluble and colloidal phases along the GA03 GEOTRACES North Atlantic Transect. Deep-Sea Res. II Top. Stud. Oceanogr. 116, 130–151.
Fitzsimmons, J.N., Bundy, R.M., Al-Subiai, S.N., Barbeau, K.A., Boyle, E.A., 2015c. The composition of dissolved iron in the dusty surface ocean: an exploration using size-fractionated iron-binding ligands. Mar. Chem. 173, 125–135.
Gerringa, L.J.A., Rijkenberg, M.J.A., Schoemann, V., Laan, P., de Baar, H.J.W., 2015. Organic complexation of iron in the West Atlantic Ocean. Mar. Chem. 177, 434–446.
Hansard, S.P., Landing, W.M., Measures, C.I., Voelker, B.M., 2009. Dissolved iron (II) in the Pacific Ocean: measurements from the PO2 and P16N CLIVAR/CO_2 repeat hydrography expeditions. Deep-Sea Res. I Oceanogr. Res. Pap. 56 (7), 1117–1129.
Hatta, M., Measures, C.I., Wu, J., Roshan, S., Fitzsimmons, J.N., Sedwick, P., Morton, P., 2015. An overview of dissolved Fe and Mn distributions during the 2010–2011 US GEOTRACES north Atlantic cruises: GEOTRACES GA03. Deep-Sea Res. II Top. Stud. Oceanogr. 116, 117–129.
Hayes, C.T., Fitzsimmons, J.N., Boyle, E.A., McGee, D., Anderson, R.F., Weisend, R., Morton, P.L., 2015. Thorium isotopes tracing the iron cycle at the Hawaii Ocean Time-series Station ALOHA. Geochim. Cosmochim. Acta 169, 1–16.
Huang, S., Rahn, K.A., Arimoto, R., Graustein, W.C., Turekian, K.K., 1999. Semiannual cycles of pollution at Bermuda. J. Geophys. Res. 104, 30,309–30,318.
Johnson, K.S., Gordon, R.M., Coale, K.H., 1997. What controls dissolved iron concentrations in the world ocean? Mar. Chem. 57 (3), 137–161.
Kadko, D., Landing, W.M., Shelley, R.U., 2015. A novel tracer technique to quantify the atmospheric flux of trace elements to remote ocean regions. J. Geophys. Res. Oceans 120 (2), 848–858.
Karl, D.M., Lukas, R., 1996. The Hawaii Ocean time-series (HOT) program: background, rationale and field implementation. Deep-Sea Res. II Top. Stud. Oceanogr. 43 (2–3), 129–156.
Karl, D., Letelier, R., Tupas, L., Dore, J., Christian, J., Hebel, D., 1997. The role of nitrogen fixation in biogeochemical cycling in the subtropical North Pacific Ocean. Nature 388 (6642), 533–538.
Kieber, R.J., Williams, K., Willey, J.D., Skrabal, S., Avery, G.B., 2001. Iron speciation in coastal rainwater: concentration and deposition to seawater. Mar. Chem. 73 (2), 83–95.
Kieber, R.J., Skrabal, S.A., Smith, B.J., Willey, J.D., 2005. Organic complexation of Fe (II) and its impact on the redox cycling of iron in rain. Environ. Sci. Technol. 39 (6), 1576–1583.
Lomas, M.W., Bates, N.R., Johnson, R.J., Knap, A.H., Steinberg, D.K., Carlson, C.A., 2013. Two decades and counting: 24-years of sustained open ocean biogeochemical measurements in the Sargasso Sea. Deep-Sea Res. II Top. Stud. Oceanogr. 93, 16–32.
Mawji, E., Schlitzer, R., Dodas, E.M., Abadie, C., Abouchami, W., Anderson, R., et al., 2015. The GEOTRACES intermediate data product 2014. Mar. Chem. 177, 1–8.
McGillicuddy, D.J., Anderson, L.A., Bates, N.R., Bibby, T., Buesseler, K.O., Carlson, C.A., et al., 2007. Eddy/wind interactions stimulate extraordinary mid-ocean plankton blooms. Science 316 (5827), 1021–1026.
Measures, C.I., Yuan, J., Resing, J.A., 1995. Determination of iron in seawater by flow injection analysis using in-line preconcentration and spectrophotometric detection. Mar. Chem. 50 (1–4), 3–12.
Michaels, A.F., Knap, A.H., 1996. Overview of the U.S. JGOFS BATS and Hydrostation S program. Deep-Sea Res. 43 (2–3), 157–198.
Millero, F.J., Sotolongo, S., Izaguirre, M., 1987. The oxidation kinetics of Fe (II) in seawater. Geochim. Cosmochim. Acta 51 (4), 793–801.
Moody, J.L., Oltsman, S.J., Levy, H., Merrill, J.T., 1995. Transport climatology of tropospheric ozone: Bermuda, 1988–1991. J. Geophys. Res. 100, 7179–7194.
Moore, C.M., Mills, M.M., Arrigo, K.R., Berman-Frank, I., Bopp, L., Boyd, P.W., et al., 2013. Processes and patterns of oceanic nutrient limitation. Nat. Geosci. 6 (9), 701–710.
Pham, A.L., Ito, T., 2018. Formation and maintenance of the GEOTRACES subsurface-dissolved iron maxima in an ocean biogeochemistry model. Glob. Biogeochem. Cycles 32 (6), 932–953.
Phillips, H.E., Joyce, T.M., 2007. Bermuda's tale of two time series: Hydrostation S and BATS. J. Phys. Oceanogr. 37 (3), 554–571.
Rijkenberg, M.J., Middag, R., Laan, P., Gerringa, L.J., van Aken, H.M., Schoemann, V., et al., 2014. The distribution of dissolved iron in the West Atlantic Ocean. PLoS One 9 (6), e101323.
Saito, M.A., Noble, A.E., Tagliabue, A., Goepfert, T.J., Lamborg, C.H., Jenkins, W.J., 2013. Slow-spreading submarine ridges in the South Atlantic as a significant oceanic iron source. Nat. Geosci. 6 (9), 775.
Sarthou, G., Bucciarelli, E., Chever, F., Hansard, S.P., Planchon, J.M., Speich, S., et al., 2011. Labile Fe (II) concentrations in the Atlantic sector of the Southern Ocean along a transect from the subtropical domain to the Weddell Sea Gyre. Biogeosciences 8, 2461–2479.
Schlitzer, R., et al., 2018. The GEOTRACES intermediate data product 2017. Chem. Geol. 493, 210–223.
Schroth, A.W., Crusius, J., Sholkovitz, E.R., Bostick, B.C., 2009. Iron solubility driven by speciation in dust sources to the ocean. Nat. Geosci. 2 (5), 337–340.
Sedwick, P.N., DiTullio, G.R., Mackey, D.J., 2000. Iron and manganese in the Ross Sea, Antarctica: seasonal iron limitation in Antarctic shelf waters. J. Geophys. Res. Oceans 105 (C5), 11321–11336.
Sedwick, P.N., Church, T.M., Bowie, A.R., Marsay, C.M., Ussher, S.J., Achilles, K.M., et al., 2005. Iron in the Sargasso Sea (Bermuda Atlantic Time-series Study region) during summer: Eolian imprint, spatiotemporal variability, and ecological implications. Glob. Biogeochem. Cycles 19 (4).
Sedwick, P.N., Sholkovitz, E.R., Church, T.M., 2007. Impact of anthropogenic combustion emissions on the fractional solubility of aerosol iron: evidence from the Sargasso Sea. Geochem. Geophys. Geosyst. 8 (10).
Sedwick, P.N., Bowie, A.R., Trull, T.W., 2008. Dissolved iron in the Australian sector of the Southern Ocean (CLIVAR SR3 section): meridional and seasonal trends. Deep-Sea Res. I Oceanogr. Res. Pap. 55 (8), 911–925.
Sedwick, P.N., Marsay, C.M., Sohst, B.M., Aguilar-Islas, A.M., Lohan, M.C., Long, M.C., et al., 2011. Early season depletion of dissolved iron in the Ross Sea polynya: implications for iron dynamics on the Antarctic continental shelf. J. Geophys. Res. Oceans 116 (C12).
Sedwick, P.N., Sohst, B.M., Ussher, S.J., Bowie, A.R., 2015. A zonal picture of the water column distribution of dissolved iron (II) during the US GEOTRACES North Atlantic transect cruise (GEOTRACES GA03). Deep-Sea Res. II Top. Stud. Oceanogr. 116, 166–175.
Shelley, R.U., Sedwick, P.N., Bibby, T.S., Cabedo-Sanz, P., Church, T.M., Johnson, R.J., et al., 2012. Controls on dissolved cobalt in surface waters of the Sargasso Sea: comparisons with iron and aluminum. Glob. Biogeochem. Cycles 26 (2). https://doi.org/10.1029/2011GB004155.
Sholkovitz, E.R., Landing, W.M., Lewis, B.L., 1994. Ocean particle chemistry: the fractionation of rare earth elements between suspended particles and seawater. Geochim. Cosmochim. Acta 58 (6), 1567–1579.
Siegel, D.A., McGillicuddy, D.J., Fields, E.A., 1999. Mesoscale eddies, satellite altimetry,

and new production in the Sargasso Sea. J. Geophys. Res. Oceans 104 (C6), 13359–13379.
Steinberg, D.K., Carlson, C.A., Bates, N.R., Johnson, R.J., Michaels, A.F., Knap, A.H., 2001. Overview of the US JGOFS Bermuda Atlantic Time-series Study (BATS): a decade-scale look at ocean biology and biogeochemistry. Deep-Sea Res. II Top. Stud. Oceanogr. 48 (8), 1405–1447.
Sunda, W.G., Huntsman, S.A., 1997. Interrelated influence of iron, light and cell size on marine phytoplankton growth. Nature 390, 389–392.
Tagliabue, A., Aumont, O., DeAth, R., Dunne, J.P., Dutkiewicz, S., Galbraith, E., et al., 2016. How well do global ocean biogeochemistry models simulate dissolved iron distributions? Glob. Biogeochem. Cycles 30 (2), 149–174.
Tagliabue, A., Bowie, A.R., Boyd, P.W., Buck, K.N., Johnson, K.S., Saito, M.A., 2017. The integral role of iron in ocean biogeochemistry. Nature 543 (7643), 51–59.
Ussher, S.J., Yaqoob, M., Achterberg, E.P., Nabi, A., Worsfold, P.J., 2005. Effect of model ligands on iron redox speciation in natural waters using flow injection with luminol chemiluminescence detection. Anal. Chem. 77 (7), 1971–1978.
Ussher, S.J., Achterberg, E.P., Sarthou, G., Laan, P., de Baar, H.J., Worsfold, P.J., 2010. Distribution of size fractionated dissolved iron in the Canary Basin. Mar. Environ. Res. 70 (1), 46–55.
Ussher, S.J., Achterberg, E.P., Powell, C., Baker, A.R., Jickells, T.D., Torres, R., Worsfold, P.J., 2013. Impact of atmospheric deposition on the contrasting iron biogeochemistry of the north and South Atlantic Ocean. Glob. Biogeochem. Cycles 27 (4), 1096–1107.
Worsfold, P.J., Achterberg, E.P., Birchill, A.J., Clough, R., Leito, I., Lohan, M.C., Milne, A., Ussher, S.J., 2019. Estimating uncertainties in oceanographic trace element measurements. Front. Mar. Sci. 5, 515.
Wu, J., Boyle, E., 2002. Iron in the Sargasso Sea: implications for the processes controlling dissolved Fe distribution in the ocean. Glob. Biogeochem. Cycles 16 (4).
Wu, J., Boyle, E., Sunda, W., Wen, L.S., 2001. Soluble and colloidal iron in the oligotrophic North Atlantic and North Pacific. Science 293 (5531), 847–849.
Wuttig, K., Wagener, T., Bressac, M., Dammshäuser, A., Streu, P., Guieu, C., Croot, P., 2013. Impacts of dust deposition on dissolved trace metal concentrations (Mn, Al and Fe) during a mesocosm experiment. Biogeosciences 10 (4), 2583–2600.